Chinese Chemical Letters 36 (2025) 109672

Contents lists available at ScienceDirect

Chinese Chemical Letters

journal homepage: www.elsevier.com/locate/cclet

Enhanced C_2H_2/CO_2 separation in tetranuclear Cu(II) cluster-based metal-organic frameworks by adjusting divider length of pore space partition

Fahui Xiang[a,b,1], Lu Li[a,1], Zhen Yuan[a], Wuji Wei[a], Xiaoqing Zheng[a], Shimin Chen[a], Yisi Yang[a], Liangji Chen[a], Zizhu Yao[a], Jianwei Fu[b], Zhangjing Zhang[a,*], Shengchang Xiang[a,*]

[a] Fujian Provincial Key Laboratory of Polymer Materials, College of Chemistry and Materials Science, Fujian Normal University Fuzhou 350108, China
[b] Institute of Quality Standards and Testing Technology for Agro-Products, Fujian Key Laboratory of Agro-Products Quality and Safety, Fujian Academy of Agricultural Sciences, Fuzhou 350001, China

ARTICLE INFO

Article history:
Received 24 December 2023
Revised 8 February 2024
Accepted 22 February 2024
Available online 8 March 2024

Keywords:
Metal-organic frameworks
Dual functionalities
Pore space partition
C_2H_2/CO_2 separation
Divider length adjustment

ABSTRACT

Achieving efficient adsorption and separation of C_2H_2/CO_2 mixtures is a goal that people have always pursued to improve the situation of high energy consumption brought by traditional separation technologies in industry today. High-nuclearity metal cluster-based MOFs with different functionalities are promising for this separation, but it is a complicated and difficult task to precisely control their structures. The strategy of pore-space partition (PSP) is a powerful way to construct this type MOFs, which has the characteristic of isostructural relationship, and can be resulted in a similar performance for them. Therefore, it is an interesting work to explore the effect of MOFs property by adjusting the size of PSP dividers. Herein, three tetranuclear Cu(II) cluster-based MOFs (**FJU-112/113/114**) with dual functionalities has been successfully obtained by PSP strategy with various lengths of divider units. With the highest microporosity and unique functional site, **FJU-114** realized a good improvement in the adsorption and separation performance of C_2H_2/CO_2. The gas adsorption and lab-scale C_2H_2/CO_2 breakthrough experiments demonstrated that **FJU-114** exhibits the highest adsorption uptake of 77 cm^3/g for C_2H_2, and shows the best separation factor of 4.2 among three MOFs. The GCMC simulation reveals that a stronger adsorption binding site of C_2H_2 in **FJU-114a** located in the cage II near the unchanged tetranuclear copper node, combined with its high microporosity to achieve the effect of dual functionalities for the improvement performance of C_2H_2 adsorption and separation.

As an emerging porous material platform with flexible design capabilities, metal-organic frameworks (MOFs) not only exhibit a variety of topological structure types, but also provide convenient and diverse ways to modify and functionalize structural pores, which attracted widespread attention from researchers in the field of gas adsorption [1–5]. In the subclass of MOFs, high-nuclearity metal cluster-based MOFs generally possess a good thermal and chemical stability [6], and they can also provide more post modification opportunities on the skeleton of materials [7–9]. However, one of the drawbacks of this subclass MOFs is their large channel limits the achievement of high selectivity for gas separation and purification. For this drawback, the strategy of pore space partition (PSP) is an effective way to narrow the channel size and improve the gas adsorption performance [2,10,11]. Our previous work also shows that the tetranuclear metal cluster-based MOFs with the method of PSP exhibits good C_2H_2 selectivity and separation performance [12]. Normally, the characteristic of isostructural relationship in these MOFs constructed by the PSP strategy can be resulted in the similar performance for them.

Although, the MOFs with the features of isostructural relationship and similar performance, we want to further explored the relationship between the gas adsorption and separation performance and the structural changes brough by adjusting the size of the PSP dividers, which has rarely been discussed before. It is amazing that the divider size regulation not only can effectively reduce the size of the pore to improve the microporosity and gas selectivity, but also change the gas adsorption sites in the

* Corresponding authors.
E-mail addresses: zzhang@fjnu.edu.cn (Z. Zhang), scxiang@fjnu.edu.cn (S. Xiang).
[1] These authors contributed equally to this work.

https://doi.org/10.1016/j.cclet.2024.109672
1001-8417/

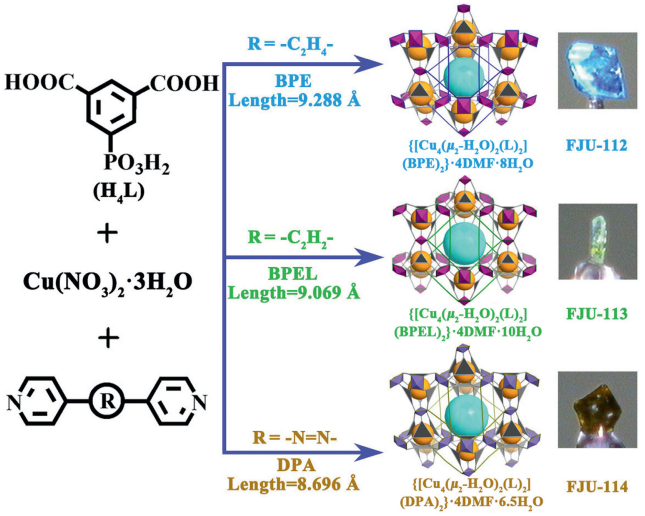

Scheme 1. The synthetic route to **FJU-112/113/114** with the various lengths of dividers BPE, BPEL and DPA, and the formula of them is {[$Cu_4(\mu_2$-$H_2O)_2(L)_2$](BPE)$_2$}·4DMF·8H_2O, {[$Cu_4(\mu_2$-$H_2O)_2(L)_2$](BPEL)$_2$}·4DMF·10H_2O, and {[$Cu_4(\mu_2$-$H_2O)_2(L)_2$](DPA)$_2$}·4DMF·6.5H_2O, respectively.

structure. Thus, three ten-connected tetranuclear copper cluster-based MOFs (**FJU-112/113/114**) have been constructed from copper salt and 3,5-dicarboxyphenylphosphonic acid (H_4L) *via* PSP strategy with various length of dividers (Scheme 1), including 1,2-bis(4-pyridyl)ethane (BPE 9.288 Å), 1,2-bis(4-pyridyl)ethylene (BPEL 9.069 Å) and 4,4′-azo-dipyridinel (DPA 9.004 Å). With the smallest length of divider unit, **FJU-114** exhibits the best adsorption and separation performance among three MOFs, which can be confirmed by its highest microporosity and a stronger functional site from the grand canonical monte carlo (GCMC) simulations. It demonstrated that controlling the length of PSP divider is an effective way to enhance the synergy effect of microporosity and functional sites in the structure to improve the gas adsorption performance of materials.

The synthesis of H_4L is referenced from the literature of Luh [13] with a slight modification. 3,5-Dicarboxylate methyl bromobenzene (2.7300 g, 10.0 mmol) and $NiCl_2$ (0.1300 g, 1.0 mmol) was placed in a two-necked round-bottom flask and heated to 170 °C under nitrogen atmosphere. After 3,5-dicarboxylate methyl bromobenzene melted and next triethyl phosphite (2.4 mL, 14.05 mmol) was added dropwise over 7 h. The mixture was heated at the same temperature and stirred overnight. Orange viscous oil was obtained and was purified by column chromatography using a 13:1 v/v mixture of ethyl acetate/ethanol. And the dimethyl 3,5-dicarboxylate-1–diethyl phenylphosphonate with colorless oil was obtain. ^{1}H NMR (DMSO–d_6, 400 MHz, ppm): δ 8.63 (1H), 8.41–8.44 (2H), 4.01–4.14 (4H), 3.933 (6H), 1.27–1.23 (6H). ^{13}C NMR (DMSO–d_6, 400 MHz, ppm): δ 164.9, 136.1, 133.4, 131.4, 130.0, 62.9, 53.3, 16.5. Dimethyl 3,5-dicarboxylate-1–diethyl phenylphosphonate were mixed with 6 mol/L hydrochloric acid by using the mole ratio of 1:6, and heated at reflux for 12 h. The white precipitate was obtained after solvent removal by rotary evaporation under vacuum conditions. And the target product 3,5-dicarboxyphenylphosphonic acid (H_4L) was obtained. The construction of the isostructural MOFs **FJU-113/114** adopts a similar method to **FJU-112** [12], $Cu(NO_3)_2{\cdot}3H_2O$ (12 mg, 0.05 mmol), H_4L (3.5 mg, 0.025 mmol), and BPEL/ DPA (4.6 mg, 0.025 mmol) were dissolved by the mixed solvents of DMF/H_2O (4/4 mL) in a 20 mL glass bottle, and put it on the open air under room temperature for three days, then crystal was obtained.

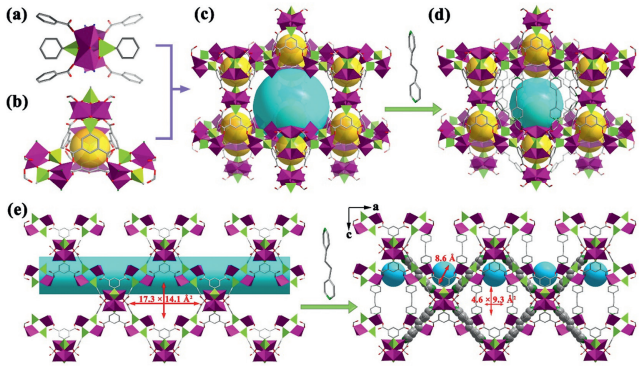

Fig. 1. (a) The main trigonal antiprism partial building units. (b) The tetrahedral cage I. (c) The ***spn*** partial frameworks formed by the split building units and triangular organic linkers. (d) Inserting linear divider into ***spn*** net to obtain **FJU-113**. (e) Side view of the 1D channel and nanocages before and after partitioning. Colour code: Cu, teal; P, pink; C, light grey; N, green; O, red. H atoms are omitted for clarity. Cages are illustrated with light orange and turquoise balls.

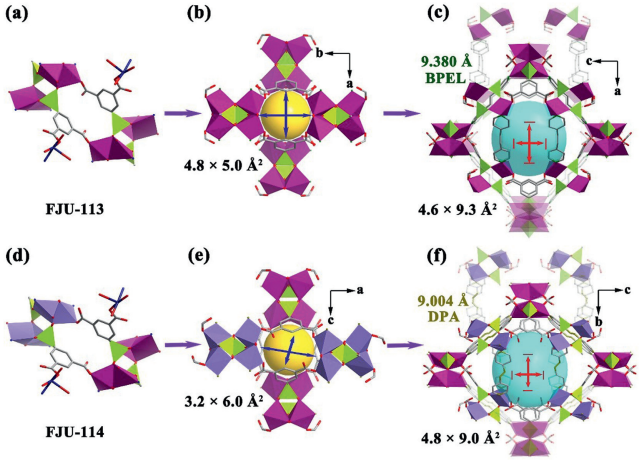

Fig. 2. (a) The tetranuclear Cu cluster node for **FJU-113**. (d) Two kinds of tetranuclear Cu cluster nodes for **FJU-114**. (b, e) Cage I and its aperture size for **FJU-113/114**, respectively. (c, f) Cage II and its aperture size for **FJU-113/114**, respectively.

Single-crystal X-ray diffraction studies revealed that green crystal **FJU-113** crystallizes in tetragonal $I4_1/amd$ space group. The size of BPEL in the lattice is stretched to 9.380 Å, close to the BPE size of 9.261 Å in **FJU-112**. **FJU-113** inherits major structural characteristic from **FJU-112** (Figs. S1a and b in Supporting information), including the ten-connected tetranuclear copper cluster node [$Cu_4(\mu_2$-$H_2O)_2N_4(PO_3)_2(CO_2)_4$] (Figs. 1a and 2a), and the connection mode between metal cluster nodes and linkers. The unique organic ligand of deprotonated L^{4-} combined with the [$Cu_4(\mu_2$-$H_2O)_2N_4(PO_3)_2(CO_2)_4$] nodes bring a structure similar to MOF-808 with a ***spn*** net [14] as one part of the main structure. The ***spn*** net contains two kinds of cages. A tetrahedral cage I centered at Wyckoff site *4a* is composed of four tetranuclear copper cluster nodes and four L^{4-}, the diameter and the channel size generated from this cage is 5.8 Å and 4.8 × 5.0 Å^2 along *b* axis (Figs. 1b and 2b, Fig. S3a in Supporting information). Cage I is connected to each other *via* sharing the tetranuclear copper cluster nodes to form the ***spn*** net with a large cage (Fig. 1c). Simultaneously, the BPEL molecules not only connect with Cu ions as another part of the host framework to enhance the stability of whole host network, but also regard as an insertion linear divider in the pore space partition (PSP) (Figs. 1d and e). The PSP has resulted in a significantly decreasing level in the window size from 17.3 × 14.1 Å^2 to 4.6 × 9.3 Å^2 along b axis. And the 1D channel of ***spn*** partial divided into nu-

merous cages (cage II, Fig. 2c) centered at Wyckoff site 8e with the diameter of 8.6 Å (Fig. 1e). Compared with the structure of **FJU-112**, the tetrahedral cage (cage I) as one part of ***spn*** partial and the cage II generated from another partial of ***2M4–1*** in **FJU-113** are almost unaffected by the divider BPEL with small dimension, resulting in the same topology and a minor change with the cage diameter size and channel aperture size. Importantly, the characteristic of cage I has four phenyls from different H_4L molecules to form a quasi-cylindrical space for the guest adsorption (Fig. S3c in Supporting information).

For **FJU-114**, as the length of 9.004 Å for the divider DPA is obviously shorter than BPE and BPEL, its space group, coordination mode of 3,5-dicarboxyphenylphosphonic anion, and the modes of the ten-connected tetranuclear copper nodes are different with those for **FJU-112/113**. The brown crystal **FJU-114** crystallizes in monoclinic *I2/a* space group, a subgroup of tetragonal $I4_1/amd$ space group, in which the asymmetric unit consists of two Cu atoms, two μ_2-H_2O, two H_4L and two DPA organic ligands, indicating that there are two kinds of 10-connected tetranuclear copper nodes (Fig. 2d) and the 3,5-dicarboxyphenylphosphonic ligand adopts two various coordination manners (Figs. S2b and d in Supporting information). Nevertheless, as the ligand DPA is also bidentate same as BPE and BPEL, the ***sp2*** topology containing ***spn*** and ***2M4–1*** subnets can be kept in **FJU-114** (Figs. S1c and d in Supporting information). Notably, due to the change of divider size, the new connection mode between nodes and ligands was presented, which significantly affect the aperture size of cage I and the 1D channel in **FJU-114**, one side of the window size was significantly narrower through the carboxylate oxygen compare to that of another side (Fig. 2e and Fig. S3b in Supporting information). Besides, the feature of cage II has two interpenetrated quasi quadrilateral parts structure which constructed by connecting two different nodes with DPA ligand to provide a guest adsorption functional site near the unchanged cluster node originating from the carboxylate oxygen O4 and the π conjugation between pyridine group and N6 (Fig. S3d in Supporting information). Among them, the length in the crystal of BPEL and DPA are obviously elongated compare to that of original molecule size to affect the change of the crystal structure. As a result, the diameter sizes of cage I and II in **FJU-114** remains 5.8 Å and 8.6 Å, but the aperture sizes of the two channels have been changed to 3.2×6.0 Å^2 along *b* axis and 4.8×9.0 Å^2 along *a* axis, respectively (Figs. 2e and f). By the calculation of PLATON program [15], the total accessible volume of **FJU-113/114** is 45.6% and 46.1%, respectively, which were filled with the disordered solvent molecules. The unit cell parameters of these MOFs are listed in Table S1 (Supporting information, CCDC: 2131130 and 2131131).

The phase purity of the as-synthesized samples of **FJU-113/114** was confirmed by a comparison of the experimental and simulated powder X-ray diffraction (PXRD) patterns (Fig. S4 in Supporting information). The structure of them was further verified by elemental analysis and thermogravimetric analysis (TGA), and their formulas are listed as follows: $\{[Cu_4(\mu_2\text{-}H_2O)_2(L)_2](BPEL)_2\}\cdot 4DMF\cdot 10H_2O$, and $\{[Cu_4(\mu_2\text{-}H_2O)_2(L)_2](DPA)_2\}\cdot 4DMF\cdot 6.5H_2O$, respectively. As shown in the TGA curves, **FJU-113/114** has a similar thermal stability up to about 250 °C, and the weight loss nearly 250 °C for them can be attributed to the solvents guest escape (Fig. S5a in Supporting information), which have further confirmed by the elemental analysis. The FT-IR spectra of the synthesized MOFs (**FJU-113/114**) are shown in Fig. S5b (Supporting information). The stretch peaks of P=O bonds are located at 971, 1064, and 1120 cm^{-1}, the stretch peaks of 1660 cm^{-1} and the range from 1570 cm^{-1} to 1660 cm^{-1} are belong to C=C and N=N bond, respectively, which can be found in **FJU-113** and **FJU-114** [16,17]. The variable temperature PXRD experiments shown that **FJU-113/114** can be remained their thermal stability up to 250 and 200 °C, respectively (Fig. S6 in Supporting information). Simultaneously, **FJU-113** can keep chemical stability under different pH range from 2 to 12, while **FJU-114** (pH from 4 to 12) is weaker than that of **FJU-113** for 24 h (Fig. S7 in Supporting information). To explore the permanent porosity, two samples were guest-exchanged by anhydrous acetone and then degassed at 30 °C under high vacuum for 32 h to yield guest-free phases **FJU-113a/114a**. The PXRD pattern of **FJU-113a/114a** revealed that the structural integrity was still preserved after activation (Fig. S4 in Supporting information).

As shown in Fig. 3a, single component N_2 adsorption at 77 K were measured on Micromeritic ASAP 2020 HD. The sorption isotherms of **FJU-113a/114a** belong to type I behaviours, and their Brunauer-Emmett-Teller (BET) surface areas are 724, and 891 m^2/g, respectively (Figure S9). The corresponding pore volumes for **FJU-113a/114a** are 0.33, and 0.35 cm^3/g, respectively, close to the theoretical values of 0.41 and 0.40 cm^3/g calculated from their crystal structures. The pore-size distribution (PSD) of **FJU-113a/114a** was analysed from the isotherms of 273 K CO_2 and 77 K N_2 based on the nonlocal density functional theory (NLDFT) model. They show narrow pore cavity sizes distributions centred at 5.8 and 8.6 Å (Fig. 3b and Fig. S8a in Supporting information), close to the cavity sizes determined from their crystal structures. Notably, the cumulative pore volume of **FJU-114a** is always higher than those of **FJU-113a** and **FJU-112a** in the range of 3.5–11 Å (Fig. 3c and Fig. S8b in Supporting information), indicating a higher microporosity in **FJU-114a**, which is further verified by comparing the micropore surface area and the micropore volume derived by *t*-plot method to BET specific surface areas and pore volumes in these MOFs (Table S2 in Supporting information). The short divider DPA makes **FJU-114a** with higher pore volume than **FJU-112a** and **FJU-113a** with the long dividers BPE and BPEL, which further make an important effect on its gas adsorption and separation performance.

These ten-connected tetranuclear copper cluster-based MOFs (**FJU-113a/114a**) with permanent porosity encourage us to explore their abilities for the adsorption and separation of C_2H_2 and CO_2. As shown in Fig. 3d, the single-component uptake of C_2H_2 (77 cm^3 (STP)/g) for **FJU-114a** is about two times higher than that of CO_2 (39 cm^3 (STP)/g) at 296 K, 1 bar. However, it is worth noting that the uptake amount of C_2H_2 for **FJU-114a** is obvious higher than that of **FJU-113a** (**FJU-112a**, Fig. S8d in Supporting information), while, the CO_2 adsorption capacity of them almost keep the same. This is mainly due to the reduction in the length of the dividers (PEL (BPE) > DPA) result in an increase of the micropore porosity in the structure of **FJU-114a** (**FJU-114a** > **FJU-113a** (**FJU-112a**)). Notably, the uptake capacity of C_2H_2 in **FJU-114a** is comparable to those MOFs of **JXNU-12** (77.9 cm^3/g) [18], **UPC-80** (77.3 cm^3/g) [19], **ZNU-1** (76.3 cm^3/g) [20], and **FJU-112a** (74 cm^3/g) [12], but smaller than **SNNU-98-Mn** (222.9 cm^3/g) [21], **ZJU-50a** (192 cm^3/g) [22], **FJU-90a** (180 cm^3/g) [11], **ZJNU-118** (159.5 cm^3/g) [23], ATC–Cu (112 cm^3/g) [24], **ZJNU-109** (104.6) [25], and **FJU-118a** (88.6 cm^3/g) [26]. These results show that these MOFs could have the potential to apply in the separation of C_2H_2/CO_2 mixture gases.

The adsorption enthalpy (Q_{st}) of **FJU-113a/114a** was calculated by virial fitting for C_2H_2 and CO_2 from the adsorption isotherms at 273 and 296 K. The calculated Q_{st} value for C_2H_2 in **FJU-113a/114a** (32.7 and 33.0 kJ/mol) is almost the same at near zero coverage (Fig. 3e, Figs. S10a and c in Supporting information). While, the Q_{st} value of CO_2 for **FJU-113a/114a** is calculated to be 26.5, and 29.1 kJ/mol, respectively (Figs. S10b, d and S11 in Supporting information), which is obviously lower than that of C_2H_2. This indicated that **FJU-13a/114a** exhibits a stronger affinity for C_2H_2 than CO_2. Compared to the reported MOF materials, the moderate C_2H_2 Q_{st} value for **FJU-114a** is significantly lower than that of NCU-100 (60.5 kJ/mol) [27], ZNU-1 (54 kJ/mol) [20], MFU-4-F (41 kJ/mol) [28], MPM-2 (38.5 kJ/mol) [29], and MFM-160a

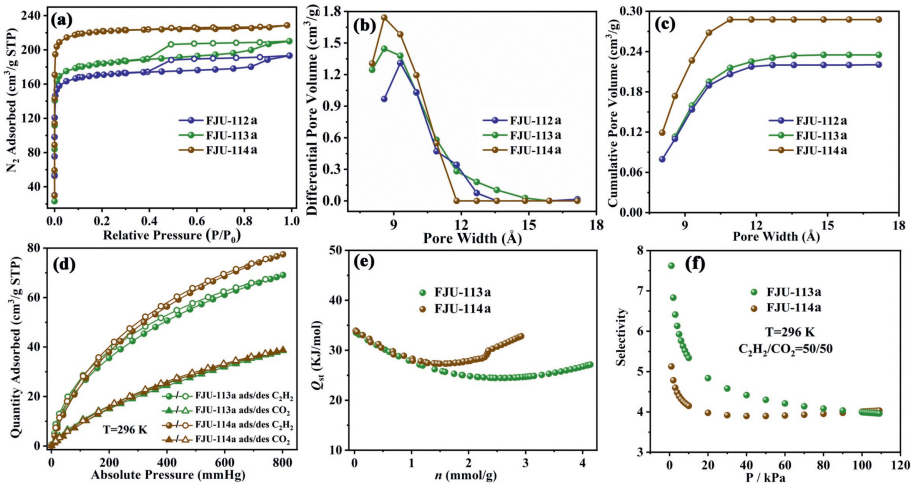

Fig. 3. (a) N_2 adsorption isotherm of **FJU-112a/113a/114a** at 77 K. (b) The pore size distribution and (c) cumulative pore volume of **FJU-112a/113a/114a** from 77 K N_2 isotherms based on the nonlocal density functional theory (NLDFT) model. (d) C_2H_2 and CO_2 adsorption isotherms of **FJU-113a/114a** at 296 K. (e) Adsorption enthalpy of C_2H_2 in **FJU-113a/114a**. (f) IAST selectivity for equivalent C_2H_2/CO_2 of **FJU-113a/114a** at 100 kPa and 296 K.

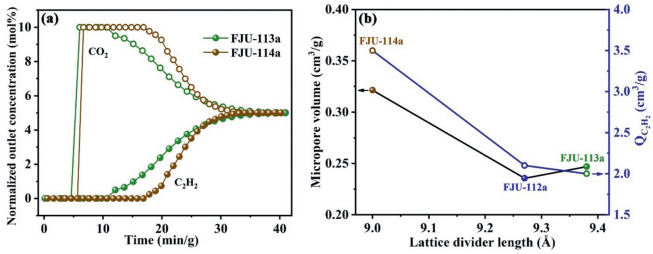

Fig. 4. (a) Experimental column breakthrough curves of **FJU-112a/113a/114a** for C_2H_2/CO_2/He (v/v/v = 5/5/90) separation at 296 K and 1 bar. (b) The relationship between lattice divider length and micropore volume and separation uptakes for **FJU-112a/113a/114a**, respectively.

(37 kJ/mol) [30]. This moderate Q_{st} for C_2H_2 provide an easier way to regenerate the materials in their practical gas adsorption and separation.

To deal with the separations of gas mixture, we first determined the C_2H_2/CO_2 separation selectivity of the **FJU-113a/114a** by means of ideal adsorbed solution theory (IAST) calculations after fitting the pure-component isotherms to the single-site Langmuir-Freundlich equation at different pressures (Fig. S12 in Supporting information). The calculated selectivity of C_2H_2/CO_2 (50:50) for **FJU-114a** is 4.0, and this value almost the same as that of **FJU-113a** (Fig. 3f). Above all, with the advantages of suitable stability, relative low adsorption enthalpies and considerable adsorption selectivity in **FJU-113a/114a**, indicated that these materials can be a promising solid absorbent candidate.

Next, a laboratory-scale fixed-bed breakthrough experiments were performed in a packed column of activated **FJU-113a/114a** to evaluate their separation performance for actual mixtures of C_2H_2/CO_2/He (5/5/90, v/v/v) at room temperature under a total flow of 2 mL/min. As shown in Fig. 4a, both **FJU-113a** and **FJU-114a** could be successfully realized the complete separation of C_2H_2 from CO_2 at ambient conditions. It can be observed that pure CO_2 was first to elute through the bed, and pure C_2H_2 was retained until the uptake capacity got saturated in both materials of **FJU-113a** and **FJU-114a**. Obviously, the breakthrough time of CO_2 for two materials is very close (6.1 and 6.7 min/g for **FJU-113a** and **FJU-114a**, respectively). On the contrary, the breakthrough time of C_2H_2 for **FJU-113a** (12.1 min/g) is earlier than that of **FJU-114a** (17.8 min/g), which means that **FJU-114a** exhibits a better separation performance than that of **FJU-113a** (**FJU-112a**). More importantly, the separation uptake for **FJU-114a** (0.35 cm^3/g) is significantly higher than that of **FJU-113a/112a** (0.21, and 0.20 cm^3/g for **FJU-112a/113a**, respectively), which could be well confirmed by the consequents of micropore volume from three MOFs (0.24, 0.25, and 0.32 cm^3/g for **FJU-112a/113a/114a**, respectively) caused by the adjustment of divider size (Fig. 4b). This means that the gas separation performance of them have closely related to the dual functionalities of high microporosity and a stronger functional site. It is worth mentioned that **FJU-114a** (4.2) has a better C_2H_2/CO_2 separation factor compared to **FJU-113a** (3.0), which can be well match with the results of adsorption performance. Furthermore, the separation factor value of C_2H_2/CO_2 in **FJU-114a** is comparable to those MOFs (Table S3 in Supporting information) including: **ZJU-74a** (4.3) [31], **ZJU-50a** (4.2) [22], Cu^I@UiO-66-$(COOH)_2$ (3.4) [32], DNL-9(Fe) (3.0) [33], **FJU-112a** (3.0) [12], and **FJU-118a** (1.9) [26], but this value is smaller than that of **ZNU-1** (49) [20], and **BSF-3** (16) [34]. Multiple cycling C_2H_2/CO_2/He dynamic breakthrough experiments were measured under the same operating conditions for these materials, showing that **FJU-113a/114a** can be maintained the retention time of C_2H_2 and CO_2 (Fig. S13 in Supporting information). It means that the adsorption capacity of both MOFs is well retained under dynamic capturing, which could be the potential candidate for C_2H_2/CO_2 mixtures separation, especially for **FJU-114a**.

To further understand the host-guest interactions, the grand canonical Monte Carlo (GCMC) simulations was employed to determine the possible position distribution of C_2H_2 (the primary binding site) in the frameworks of **FJU-112a/113a/114a**. Compared to the primary binding site located in cage I for **FJU-112a** (Figs. 5a and b), the primary binding site of **FJU-113a** shows the same result, also located in the tetrahedral cage I (Figs. 5c and d) with multiple $\pi\cdots\pi$ interactions (distance range from 3.523 Å to 3.526 Å), which mainly due to the similar size of divider in **FJU-112a/113a**. Different from **FJU-113a**, the primary binding site of **FJU-114a** located near the unchanged ten-connected tetranuclear copper node and the DPA ligand in cage II, which provide the interactions of $O^{\delta-}\cdots C^{\delta+}$ and $\pi\cdots\pi$ with the distance range of 3.363–3.636 Å (Figs. 5e and F). Because a significantly shorter size of divider (DPA) results in one side of cage I aperture size become narrower to hinder the C_2H_2 molecule enter the cage space entirely to reduce the interaction intensity between guest and host framework (Fig. S3b in Supporting information). Therefore, the primary binding site

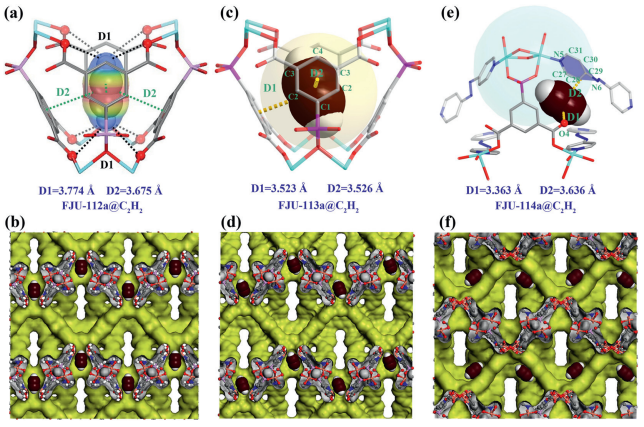

Fig. 5. (a, c, e) Calculated primary adsorption binding sites of C_2H_2 in **FJU-112a/113a/114a**. (b, d, f) Top views of the packing diagram of one C_2H_2 loaded in **FJU-112a/113a/114a**. The framework and pore surface are shown in gray and light yellow. (Color code: Cu, turquoise; O, red; C, gray; P, pink; H, white. Only the H atoms in C_2H_2 molecules are shown for clarity).

changes from cage I in **FJU-113a** to cage II in **FJU-114a**. These results indicated that **FJU-114a** with a stronger binding site interaction and higher microporosity makes an enhancement performance of gas adsorption and separation by regulating the length of divider.

In summary, we have realized the construction of three MOFs (**FJU-112/113/114**) with different gas adsorption and separation performance by the PSP strategy with variable divider length. Although it is generally believed that the MOFs constructed by the PSP strategy have the characteristics of isostructural relationship and similar performance, the adjustment of the MOF structure is achieved by adjusting the size of the PSP dividers, which has a significant impact on the separation selectivity and adsorption sites of the material for C_2H_2. With the shortest length of divider ligand, **FJU-114a** shows the highest adsorption capacity of 77 cm^3/g for C_2H_2 at 296 K 1 bar, and exhibits the best separation performance of C_2H_2/CO_2/He (v/v/v = 5/5/90) with the separation factor of 4.2. The GCMC simulation reveals that a stronger adsorption binding site of C_2H_2 in **FJU-114a** located in the cage II near the unchanged tetranuclear copper node. These results confirmed that **FJU-114a** with dual functionalities could be a potential candidate for C_2H_2/CO_2 mixtures separation. In short, the PSP strategy with various size of divider is a powerful way to realize the maximizing effects of multifunctional synergy of microporosity and adsorption binding site to improve the performance of gas adsorption and separation.

Declaration of competing interest

The authors declare that they have no known competing financial interests or personal relationships that could have appeared to influence the work reported in this paper.

Acknowledgments

This work was financially supported by the National Natural Science Foundation of China (Nos. 21975044, 21971038, 21922810 and 22271046), the Fujian Provincial Department of Science and Technology (Nos. 2023J01355, 2023J011106 and 2022R1022001).

Supplementary materials

Supplementary material associated with this article can be found, in the online version, at doi:10.1016/j.cclet.2024.109672.

References

[1] S. Yuan, L. Huang, Z. Huang, et al., J. Am. Chem. Soc. 142 (2020) 4732–4738.
[2] L. Liu, Z. Yao, Y. Ye, et al., J. Am. Chem. Soc. 142 (2020) 9258–9266.
[3] Q. Yu, L. Guo, D. Lai, et al., Sep. Purif. Technol. 268 (2021) 118646.
[4] U. Ryu, S. Jee, P.C. Rao, et al., Coord. Chem. Rev. 426 (2021) 213544.
[5] X. Zheng, L. Chen, H. Zhang, et al., Angew. Chem. Int. Ed. 62 (2023) e202216710.
[6] J.H. Cavka, S. Jakobsen, U. Olsbye, et al., J. Am. Chem. Soc. 130 (2008) 13850–13851.
[7] H. Li, L. Li, R.B. Lin, et al., ACS Sustainable Chem. Eng. 7 (2019) 4897–4902.
[8] H.M. Wen, M. Liu, Y. Ling, et al., J. Mater. Chem. A 11 (2023) 17821–17827.
[9] A. Sharma, J. Lim, S. Jeong, et al., Angew. Chem. Int. Ed. 60 (2021) 14334–14338.
[10] X. Zhao, X. Bu, Q.G. Zhai, H. Tran, P. Feng, J. Am. Chem. Soc. 137 (2015) 1396–1399.
[11] Y. Ye, Z. Ma, R.B. Lin, et al., J. Am. Chem. Soc. 141 (2019) 4130–4136.
[12] F. Xiang, H. Zhang, Y. Yang, et al., Angew. Chem. Int. Ed. 62 (2023) e202300638.
[13] C.Y. Lo, C.H. Chen, T.W.T. Tsai, et al., J. Chin. Chem. Soc. 57 (2010) 539–546.
[14] H. Furukawa, F. Gándara, Y.B. Zhang, et al., J. Am. Chem. Soc. 136 (2014) 4369–4381.
[15] A.L. Spek, PLATON, A Multipurpose Crystallographic Tool, Utrecht University, 2001.
[16] E. Pretsch, P. Bühlmann, M. Badertscher, Structure Determination of Organic Compounds: Tables of Spectral Data, Springer-Verlag Berlin Heidelberg, 2009, p. 174.
[17] Y. Zhang, L. Wang, J. Hu, et al., CrystEngComm 22 (2020) 2649–2655.
[18] X.P. Fu, Y.L. Wang, X.F. Zhang, et al., Chem. Eng. J. 432 (2022) 134433.
[19] C. Jiang, C. Hao, X. Wang, et al., Chem. Eng. J. 453 (2023) 139713.
[20] L. Wang, W. Sun, Y. Zhang, et al., Angew. Chem. Int. Ed. 60 (2021) 22865–22870.
[21] J.W. Wang, S.C. Fan, H.P. Li, et al., Angew. Chem. Int. Ed. 62 (2023) e202217839.
[22] K. Shao, H.M. Wen, C.C. Liang, et al., Angew. Chem. Int. Ed. 61 (2022) e202211523.
[23] L. Fan, L. Yue, W. Sun, et al., ACS Appl. Mater. Inter. 13 (2021) 40788–40797.
[24] Z. Niu, X. Cui, T. Pham, et al., Angew. Chem. Int. Ed. 60 (2021) 5283–5288.
[25] T. Xu, M. He, L. Fan, et al., Dalton Trans. 50 (2021) 638–646.
[26] Q. Song, Y. Yang, F. Yuan, et al., J. Mater. Chem. A 10 (2022) 9363–9369.
[27] J. Wang, Y. Zhang, Y. Su, et al., Nat. Commun. 13 (2022) 200.
[28] Q. Liu, S.G. Cho, J. Hilliard, et al., Angew. Chem. Int. Ed. 62 (2023) e202218854.
[29] M.Y. Gao, D. Sensharma, A.A.A. Bezrukov, et al., Small 19 (2023) 2206945.
[30] W.J.F. Trenholme, D.I. Kolokolov, M. Bound, et al., J. Am. Chem. Soc. 143 (2021) 3348–3358.
[31] J. Pei, K. Shao, J.X. Wang, et al., Adv. Mater. 32 (2020) 1908275.
[32] L. Zhang, K. Jiang, L. Yang, et al., Angew. Chem. Int. Ed. 60 (2021) 15995–16002.
[33] Y.M. Gu, Y.Y. Yuan, C.L. Chen, et al., Chem. Sci. 14 (2023) 1472–1478.
[34] Y. Zhang, J. Hu, R. Krishna, et al., Angew. Chem. Int. Ed. 59 (2020) 17664–17669.